Non-sequential optimization technique for a computer controlled optical surfacing process using multiple tool influence functions

Dae Wook Kim,[1]* Sug-Whan Kim[2] and James H. Burge[1]

[1]*College of Optical Sciences, University of Arizona, 1630 E. University Blvd, Tucson, Arizona 85721, USA*
[2]*Space Optics Laboratory, Dept. of Astronomy, Yonsei University, 134 Sinchon-dong, Seodaemun-gu, Seoul 120-749, Republic of Korea*
*letter2dwk@hotmail.com

Abstract: Optical surfaces can be accurately figured by computer controlled optical surfacing (CCOS) that uses well characterized sub-diameter polishing tools driven by numerically controlled (NC) machines. The motion of the polishing tool is optimized to vary the dwell time of the polisher on the workpiece according to the desired removal and the calibrated tool influence function (TIF). Operating CCOS with small and very well characterized TIF achieves excellent performance, but it takes a long time. This overall polishing time can be reduced by performing sequential polishing runs that start with large tools and finish with smaller tools. In this paper we present a variation of this technique that uses a set of different size TIFs, but the optimization is performed globally – *i.e.* simultaneously optimizing the dwell times and tool shapes for the entire set of polishing runs. So the actual polishing runs will be sequential, but the optimization is comprehensive. As the optimization is modified from the classical method to the comprehensive non-sequential algorithm, the performance improvement is significant. For representative polishing runs we show figuring efficiency improvement from ~88% to ~98% in terms of residual RMS (root-mean-square) surface error and from ~47% to ~89% in terms of residual RMS slope error.

©2009 Optical Society of America

OCIS codes: (220.0220) Optical design and fabrication; (220.4610) Optical fabrication; (220.5450) Polishing

References and links

1. R. A. Jones, "Computer control for grinding and polishing," Photon. Spectra •••, 34–39 (1963).
2. R. Aspden, R. McDonough, and F. R. Nitchie, Jr., "Computer assisted optical surfacing," Appl. Opt. **11**(12), 2739–2747 (1972).
3. R. E. Wagner, and R. R. Shannon, "Fabrication of aspherics using a mathematical model for material removal," Appl. Opt. **13**(7), 1683–1689 (1974).
4. R. A. Jones, "Computer-controlled polishing of telescope mirror segments," Opt. Eng. **22**, 236–240 (1983).
5. R. A. Jones, "Computer-controlled optical surfacing with orbital tool motion," Opt. Eng. **25**, 785–790 (1986).
6. J. R. Johnson, and E. Waluschka, "Optical fabrication-process modeling-analysis tool box," in *Manufacturing and metrology tooling for the Solar-A Soft X-Ray Telescope*, W.R. Sigman, L.V. Burns, C.G. Hull-Allen, A.F. Slomba, and R.G. Kusha, eds., Proc. SPIE **1333,** 106–117 (1990).
7. D. D. Walker, D. Brooks, A. King, R. Freeman, R. Morton, G. McCavana, and S. W. Kim, "The 'Precessions' tooling for polishing and figuring flat, spherical and aspheric surfaces," Opt. Express **11**(8), 958–964 (2003).
8. H. M. Pollicove, E. M. Fess, and J. M. Schoen, "Deterministic manufacturing processes for precision optical surfaces," in *Window and Dome Technologies VIII*, R. W. Tustison, eds., Proc. SPIE **5078**, 90–96 (2003).
9. D. W. Kim, and S. W. Kim, "Static tool influence function for fabrication simulation of hexagonal mirror segments for extremely large telescopes," Opt. Express **13**(3), 910–917 (2005).
10. S. D. Jacobs, "International innovations in optical finishing," in Current Developments in *Lens Design and Optical Engineering V*, P.Z. Mouroulis, W.J. Smith, and R.B. Johnson, eds., Proc. SPIE **5523,** 264–272 (2004).
11. J. H. Burge, S. Benjamin, D. Caywood, C. Noble, M. Novak, C. Oh, R. Parks, B. Smith, P. Su, M. Valente, and C. Zhao, "Fabrication and testing of 1.4-m convex off-axis aspheric optical surfaces," in *Optical Manufacturing and Testing VIII*, J. H. Burge; O. W. Fähnle and R. Williamson, eds., Proc. SPIE **7426**, 74260L1–12 (2009).

12. M. Johns, "The Giant Magellan Telescope (GMT)," in *Extremely Large Telescopes: Which Wavelengths?* T. E. Andersen, eds., Proc. SPIE **6986**, 698603 1–12 (2008).
13. J. Nelson, and G. H. Sanders, "The status of the Thirty Meter Telescope project," in *Ground-based and Airborne Telescopes II*, L. M. Stepp and R. Gilmozzi, eds., Proc. SPIE **7012**, 70121A1–18 (2008).
14. D. D. Walker, A. P. Doel, R. G. Bingham, D. Brooks, A. M. King, G. Peggs, B. Hughes, S. Oldfield, C. Dorn, H. McAndrews, G. Dando, and D. Riley, "Design Study Report: The Primary and Secondary Mirrors for the Proposed Euro50 Telescope" (2002), *http://www.zeeko.co.uk/papers/dl/New%20Study%20Report%20V%2026.pdf*.
15. T. Andersen, A. L. Ardeberg, J. Beckers, A. Goncharov, M. Owner-Petersen, H. Riewaldt, R. Snel, and D. Walker, "The Euro50 Extremely Large Telescope," in *Future Giant Telescopes*, J.R.P. Angel and R. Gilmozzi, eds., Proc. SPIE **4840**, 214–225 (2003).
16. A. Ardeberg, T. Andersen, J. Beckers, M. Browne, A. Enmark, P. Knutsson, and M. Owner-Petersen, "From Euro50 towards a European ELT," in *Ground-based and Airborne Telescopes*, L. M. Stepp, eds., Proc. SPIE **6267**, 626725 1–10 (2006).
17. R. E. Parks, "Specifications: Figure and Finish are not enough," in *An optical Believe It or Not: Key Lessons Learned*, M. A. Kahan, eds., Proc. SPIE **7071**, 70710B1–9 (2008).
18. J. M. Hill, "Optical Design, Error Budget and Specifications for the Columbus Project Telescope," in *Advanced Technology Optical Telescopes IV*, L. D. Barr, eds., Proc. SPIE **1236**, 86–107 (1990).
19. D. W. Kim, W. H. Park, S. W. Kim, and J. H. Burge, "Parametric modeling of edge effects for polishing tool influence functions," Opt. Express **17**(7), 5656–5665 (2009).
20. A. P. Bogodanov, "Optimizing the technological process of automated grinding and polishing of high-precision large optical elements with a small tool," Sov. J. Opt. Technol. **52**, 409–413 (1985).
21. C. L. Carnal, C. M. Egert, and K. W. Hylton, "Advanced matrix-based algorithms for ion beam milling of optical components," in *Current Developments in Optical Design and Optical Engineering II*, R. E. Fischer and W. J. Smith, eds., Proc. SPIE **1752**, 54–62 (1992).
22. M. Negishi, M. Ando, M. Takimoto, A. Deguchi, and N. Nakamura, "Studies on super-smooth polishing (2nd report)," J. Jpn. Soc. Precis. Eng. **62**, 408–412 (1996).
23. H. Lee, and M. Yang, "Dwell time algorithm for computer-controlled polishing of small axis-symmetrical aspherical lens mold," Opt. Eng. **40**(9), 1936–1943 (2001).
24. W. H. Press, B. P. Flannery, S. A. Teukolsky, and W. T. Vetterling, *Numerical recipes in C* (Cambridge, 1988)
25. C. Bob, Crawford, Don Loomis, Norm Schenck, and Bill Anderson, Optical Engineering and Fabrication Facility, University of Arizona, 1630 E. University Blvd, Tucson, Arizona 85721, (personal communication, 2008).
26. D. W. Kim, W. H. Park, S. W. Kim, and J. H. Burge, "Edge tool influence function library using the parametric edge model for computer controlled optical surfacing," in *Optical Manufacturing and Testing VIII*, J. H. Burge; O. W. Fähnle and R. Williamson, Proc. SPIE **7426**, 74260G1–12 (2009).
27. P. R. Goode, C. J. Denker, L. I. Didkovsky, J. R. Kuhn, and H. Wang, "1.6 m Solar Telescope in Big Bear – the NST," J. Korean Astron. Soc. **35**, 1–8 (2002).
28. A. Heller, "Safe and sustainable energy with LIFE" (2009), *https://str.llnl.gov/AprMay09/pdfs/05.09.02.pdf*.
29. H. H. Barrett, and K. J. Myers, *Foundations of Image Science* (Wiley, 2004)
30. D. W. Kim, and S. W. Kim, "Novel simulation technique for efficient fabrication of 2m class hexagonal segments for extremely large telescope primary mirrors," in *Optical Design and Testing II*, Y. Wang, Z. Weng, S. Ye and J. M. Sasian, eds., Proc. SPIE **5638**, 48–59 (2005).

1. Introduction

Many computer controlled optical surfacing (CCOS) processes have been developed and used since 1963 [1–8]. These CCOS processes are usually aimed at three characteristics, i) low tooling overhead, ii) deterministic material removal and iii) embedded process control intelligence [9,10].

These CCOS techniques have been successfully used for fabrication of large aspheric optical surfaces, including off-axis segments [4–8,11]. Nevertheless, further development in the efficiency and performance of the CCOS techniques is highly desired to meet the demanding target specifications of the next generation Extremely Large Telescope (ELT) projects, such as those for Giant Magellan Telescope (GMT), Thirty Meter Telescope (TMT), and European Extremely Large Telescope (EELT) [12–16].

Those ELTs use giant segmented primary mirrors with hundreds of square meter collecting area, and may have hundreds of segments. Each meter-class segment is to have the surface form accuracy of better than 18nm peak-to-valley [14]. Such a primary mirror system is to be phased and aligned to the precision of about 10-20nm RMS (root-mean-square) [15]. Also, mid-spatial frequency error (*a.k.a.* tool marks) suppression on these precision optical surfaces is important for maximum performance (*i.e.* less scattering, well defined point spread function) of the optical systems [17]. Most of the recent large optical surfaces have been

polished until the spatial frequencies of the surface errors satisfied a target structure function or power spectrum density (PSD) specification to quantify the target form accuracy as a function of spatial frequencies [17,18]. Thus, the improved CCOS technique must provide an efficient fabrication process for a mass-fabrication of precision optical surfaces while minimizing the mid-spatial frequency error.

In a conventional CCOS process, a dwell time map (*i.e.* ablation time as a function of position on the workpiece) of a tool influence function (TIF) is optimized as the major optimization parameter to achieve a target material removal (*i.e.* target error map). The TIF represents instantaneous material removal for a tool with specific motion. Then a numerically controlled polishing machine executes the optimized dwell time map on the workpiece by altering the transverse speed of the tool [1–7].

The convergence rate and overall efficiency of CCOS figuring are optimized using a sequence of polishing runs, where the largest scale irregularities are addressed by large tools. Smaller tools are used to correct small scale irregularities and tool marks from the larger tools. This method works, but may not be optimal.

The new CCOS process suggested here uses a non-sequential optimization technique utilizing multiple TIFs simultaneously in a single CCOS run optimization, while the conventional CCOS processes use TIFs one by one in a sequential manner. The actual polishing runs are still to be sequential under the guidance of comprehensive optimization. This new technique, which enables the ensemble of various TIFs, forms an attractive solution for the mass fabrication capability of high quality optical surfaces.

The theoretical background for the non-sequential optimization technique is presented in Section 2. We introduce, in Section 3, the non-sequential optimization engine in detail, and discuss its novelty over the conventional methods. A reference TIF library (*i.e.* collection of different TIFs) is provided also. Simulation results are presented to demonstrate the performance of the new technique in Section 4. Section 5 summarizes the implications.

2. Theoretical background

2.1 Generation of the TIF library

A TIF is the material removal foot-print for a given tool and tool motion, which can be calculated based on Preston's equation [9], but is usually measured directly. Because the material removal process is affected by the workpiece motion and edge effects, which are the function of tool position on the workpiece, the TIF is also changed according to its center position on the workpiece [19]. For instance, the relative motion between the tool and workpiece varies as the tool moves on the workpiece. Also, the tool removes more material near the workpiece edge as the tool overhangs the workpiece [19].

We define a TIF library as a collection of these TIFs depending on tool shape, tool motion, and lap materials. The TIFs are parameterized as functions of positions on the workpiece. The shape, size and magnitude of the TIFs are directly calculated from these tool configuration parameters. Two common edge TIFs from a circular tool with orbital and spin tool motion are depicted in Fig. 1 [19]. The TIF library for various tool configuration cases is provided in Appendix A.
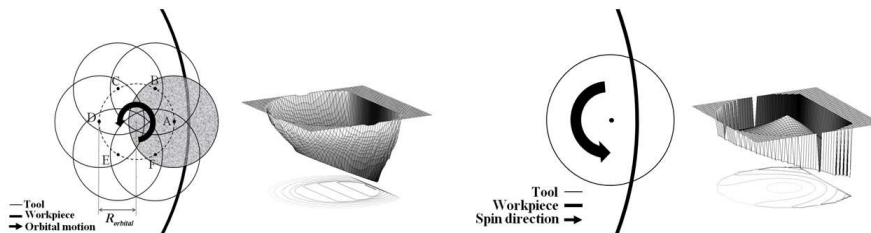

Fig. 1. Orbital (left) and spin (right) tool motion with their parametric edge TIFs [19].

2.2 Dwell time map optimization using merit functions

One key factor of successful CCOS processes is the dwell time optimization technique which provides the closest (ideally equal) removal map to the target removal map (*e.g.* measured errors on the optical surface). This optimization is also known as a de-convolution of the target removal map using a TIF. A TIF can be regarded as an impulse response of a tool with a given tool motion. In other words, a TIF represents the instantaneous material removal for a unit time at a location on the workpiece. The removal map (*i.e.* accumulated TIFs over the whole workpiece) after the tool finishes its path on the workpiece can be expressed as

$$
\begin{aligned}
&Removal\_map(x_{workpiece}, y_{workpiece}) \\
&= Dwell\_time\_map(x_{workpiece}, y_{workpiece}) ** TIF(x_{TIF}, y_{TIF}, x_{workpiece}, y_{workpiece})
\end{aligned}
\tag{1}
$$

where $x_{workpiece}$, $y_{workpiece}$ are the coordinates on the workpiece, x_{TIF}, y_{TIF} the coordinates on the TIF, and ** is the two dimensional convolution operator.

Because no general solution to the dwell time map in Eq. (1) exists, as briefly explained in Appendix B, finding the best dwell time map solution becomes an optimization problem. There has been a wide range of study for dwell time map optimization techniques (*e.g.* Fourier transform based algorithms, matrix-based least-squares algorithms) [20–23]. For all optimization techniques, it is very important to define a relevant merit function (*i.e.* objective function) to search for the optimal solution. The merit function for the non-sequential optimization technique is presented in Section 3.4.

3. Non-sequential optimization technique using multiple TIFs

3.1 Conventional (i.e. sequential) vs. non-sequential optimization technique

For the case of conventional (*i.e.* sequential) CCOS optimization, a dwell time map for one TIF has been the major search space for the optimal solution. In other words, an optimization engine searches for the optimal dwell time values for a TIF on the workpiece, which gives the best residual error map. After the CCOS run is executed, another (or same) TIF is used for the next dwell time map optimization to attack the residual error map. This sequential process is repeated, usually using successively smaller TIFs until the target specification is achieved.

In contrast, the non-sequential optimization approach uses various TIFs in a single optimization, simultaneously. Each TIF has its own dwell time map. Thus, multiple dwell time maps are brought into the non-sequential optimization engine, and optimized to achieve the target removal map. The total removal comes from the combination of all different TIFs and their own dwell time maps. Unlike the conventional technique using TIFs sequentially, different TIFs are used together to support each other in a single optimization. Non-linear optimization allows TIFs with low significance (*i.e.* ignorable dwell time or removal) to be extracted from the TIF library during the optimization. However, the key difference of the non-sequential technique from the conventional one is not the number of utilized TIFs. The conventional case may use as many TIFs as the non-sequential case in sequential manner. The major improvement comes from considering all TIFs at the same time, so that the optimal combinations of TIFs are used in constructive manner to improve the performance of the CCOS process.

For instance, a large square tool with orbital tool motion may be selected to remove most of the low spatial frequency errors on the workpiece. A small TIF from a circular tool with spin tool motion may be chosen with the large square tool TIF as an optimal set to achieve high figuring efficiency (defined in Section 4.1) by removing localized small errors. As a result, the mid-spatial frequency error on the workpiece, often caused by the small tool, can be minimized because the small tool was used only for a short time. Some specialized TIFs such as the parametric edge TIFs in Fig. 1 may be utilized for an edge figuring optimization.

In summary, both conventional and non-sequential optimization techniques are used to find an optimal dwell time map solution. However, there are significant differences, which make the non-sequential technique more powerful than the conventional one. The

optimization engine now has wider search space, including tool shape, tool size, tool motion, and so forth. These various tool configuration parameters were formerly the human's decision in the conventional CCOS technique. Many different combinations of the various TIFs are simulated to find an optimal TIF set. This technical advance leads to improvements in figuring efficiency and mid-spatial frequency error reduction, which are demonstrated in Section 4.

3.2 Non-sequential optimization engine using the gradient search method

The non-sequential optimization engine was developed using the gradient search (*a.k.a.* steepest descent) method [24]. The method is known as one of the most simple and straight forward optimization technique which works in search spaces of any number of dimensions. This method presupposes that the gradient of the merit function space at a given point can be computed. It starts at a point, and moves to the next point by minimizing a figure of merit along the line extending from the initial point in the direction of the downhill gradient. This procedure is repeated as many times as required. Because the search space for the non-sequential optimization also has multiple dimensions (*i.e.* many TIFs with various tool configuration parameters), the gradient descent method is suitable for our application.

There are two general weaknesses in the gradient descent method. First, it may take many iterations to converge towards the optimal solution in the search space, especially if the search space has complex variations [24]. This problem can be minimized by putting only reasonable TIFs in the TIF library. For instance, if we put a too small TIF (*e.g.* 5cm in diameter) in the TIF library to optimize an 8m diameter target removal map, the curvature of the figure of merit values along the 5cm TIF direction may be very shallow compared to the other reasonable size TIF (*e.g.* 20, 35, or 50cm in diameter) directions. Thus, including a 5cm TIF to the TIF library is inappropriate in this case. Limiting the total number of TIFs in the library improves computing efficiency. We do not rely on especially powerful computers for this work. Most of the optimization runs (including the case study runs in Section 4) are finished in 2-10 minutes on a regular desktop PC. Second, an improper perturbation step to calculate the local gradient may result in poor optimization performance. However, most of the search space dimensions are not a continuous space, but a discrete space depending on the given TIF library. For instance, there are only five available tool sizes (30, 40, 50, 60, and 70cm) in the reference TIF library in Table 3 (Appendix A). Although we carefully claim that the gradient descent method is suitable for this application, we still acknowledge the possibility of undesired optimization results for some special cases. For example, the TIFs are not orthogonal functions. Consequentially, the sequential application of TIFs for the optimization engine may not lead to the global minimum, but to a local minimum. However, we have not yet observed such cases in our trial optimization runs. Some actual optimization results using this optimization method are demonstrated in Section 4.

The schematic flow chart for the non-sequential optimization technique is shown in Fig. 2. The TIF library is fed into the non-sequential optimization engine to calculate the optimal dwell time maps for each TIF. More explanation about the TIF library is presented in Section 3.3. In order to calculate the local gradient in the multi-dimensional search space, the optimization engine begins to perturb the dwell time maps, which have a constant value initially. A minimum dwell time is applied during the perturbations to avoid an impractically small dwell time at a position on the workpiece. Because an actual computer controlled polishing machine (CCPM) has its mechanical limitations (*e.g.* maximum acceleration), the minimum dwell time is set by the CCPM specification. The optimization engine evaluates each TIF to achieve the target removal map for all possible TIF locations on the workpiece. For each trial, the change in the total figure of merit, FOM_{total} in Section 3.4, is recorded to determine the steepest descent case as follows. Using the TIFs with their own dwell time maps for each perturbation case, the expected removal maps are calculated using Eq. (1). The difference between the total expected removal map (*i.e.* sum of all expected removal maps from each TIF) and the target removal map is the residual error map. This residual error map is used to evaluate the FOM_{total}. After all TIFs (*i.e.* dimensions of the search space) have been

tried, the optimization engine updates the dwell time maps with the optimal trial, which recorded the steepest improvements in FOM_{total}.
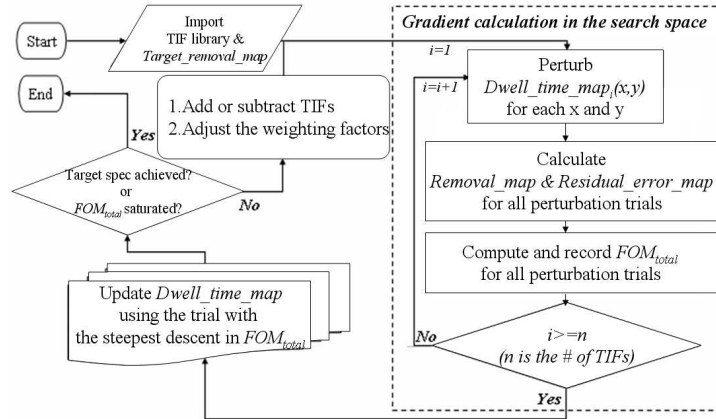

Fig. 2. Flow chart for the non-sequential optimization technique using the gradient descent method

The optimization engine repeats this procedure in a loop until FOM_{total} reaches the specification or does not decrease anymore (*i.e.* saturated). The current dwell time maps for each TIF become the optimization result. If these conditions are not met, more TIFs are fed into the TIF library. The TIFs which were hardly used are extracted from the TIF library. By performing more rounds of optimization using the updated TIF library, the optimal TIF set with their dwell time maps is determined eventually.

3.3 TIF library

The search space, including the tool configuration parameters, is defined by the TIF library in practice. Even though infinite numbers of TIFs are possible in theory, the non-sequential optimization engine utilizes the TIFs provided in the library. For instance, a typical pitch tool can be carved into any shape [25]. However, due to the limited resources (*e.g.* computing power, time), only reasonable TIFs need to be generated and saved in the library. A square tool, a circular tool, and a sector tool (*e.g.* TIF #7 in Fig. 6, Appendix A) with orbital or spin tool motions may create a sufficient tool shape search space (*i.e.* TIF library) for most cases. Also, the shop does not need to have a large inventory for all tools in the library. Only some optimal tool sets need to be made and maintained.

A complimentary TIF library was generated and provided using various tool shapes, tool motions, and tool sizes as mentioned in Section 2.1. The TIF library can be used as a good reference when one designs a CCOS run using multiple TIFs. The relative rotation speed between the tool and workpiece was changed since it played an important role to determine the TIF shape. These parameters for the TIF library are listed in Table 3 (Appendix A). The tool shape with its static TIF and ring TIF profiles are presented in Fig. 6 (Appendix A). The static TIF shows a material removal map under the tool motion for a unit time without any workpiece motion (*i.e.* workpiece RPM = 0). The ring TIF is the axisymmetric removal profile when the workpiece also rotates, and is calculated using the relative speed between the tool motion and the workpiece rotation. The ring TIF looks like a ring (*i.e.* donut) on the workpiece. The ring TIF shape is a function of radial position of the TIF center, ρ, on the workpiece. The ring TIF radial profiles in Fig. 6 are only displayed for ρ = 50, 150, and 250cm. The full TIF library includes the ring TIFs for all ρ values on the workpiece. These two different types of TIFs can be selected depending on the relative speed between the tool and workpiece. If the workpiece motion is slow compared to the tool motion, the static TIFs are used because their shapes do not change significantly by the workpiece motion. However,

if the workpiece rotates quickly, then the ring TIFs, which incorporate the workpiece motion effect, are used.

Different tool shapes (circle, ellipse, square, sector and so forth) with different tool motions (spin and orbital) were used to generate the TIF library No.1-10. The relative speed between the tool and workpiece motion was changed in TIF library No. 11-20. As shown in the ring TIFs, the removal profiles can be skewed by changing the relative rotation directions between the tool and workpiece. This technique has been often used to correct the edge errors by opticians manually [25]. The circular tool diameter was changed from 70cm to 30cm to show the effect of the tool size in TIF size and magnitude. These TIFs are shown in TIF library No. 21-25. Some TIFs using the parametric edge TIF models [19] are presented in TIF library No. 26-30. More parametric edge TIFs are available in the previous study [26].

3.4 Merit functions for the non-sequential optimization technique

The non-sequential optimization technique provides an optimal solution which suppresses the mid-spatial frequency error while still maintaining the high figuring efficiency as mentioned in Section 3.1. In order to find the optimal solution, the merit functions must completely represent the residual error map in terms of the RMS of the error map, mid-spatial frequency error, and newly generated local error features. Also, the computational load for the merit function calculations should be minimized, because the calculations are placed in the optimization loop.

The figure of merit used for this work combines six different merit functions using RSS (root-sum-square) as follows:

$$FOM_{total} \equiv RSS_{RMS\_errors} = \sqrt{\sum_{i=1}^{6} C_i \cdot FOM_i^2} \qquad (2)$$

where C_{1-6} is the weighting factors for FOM_{1-6}. Each FOM_i is defined as

$$FOM_1 \equiv RMS \ of \ Positive \ Error \ Map = \sqrt{\iint_{M+} \{error\_map(x,y)\}^2 \, dxdy \Big/ \iint_{M} dxdy} \quad (3)$$

$$FOM_2 \equiv RMS \ of \ Negative \ Error \ Map = \sqrt{\iint_{M-} \{error\_map(x,y)\}^2 \, dxdy \Big/ \iint_{M} dxdy} \quad (4)$$

$$FOM_3 \equiv RMS \ of \ x \ Slope \ Map = \sqrt{\iint_{M} \{\frac{\partial}{\partial x} error\_map(x,y)\}^2 \, dxdy \Big/ \iint_{M} dxdy} \quad (5)$$

$$FOM_4 \equiv RMS \ of \ y \ Slope \ Map = \sqrt{\iint_{M} \{\frac{\partial}{\partial y} error\_map(x,y)\}^2 \, dxdy \Big/ \iint_{M} dxdy} \quad (6)$$

$$FOM_5 \equiv RMS \ of \ x \ Curvature \ Map = \sqrt{\iint_{M} \{\frac{\partial^2}{\partial x^2} error\_map(x,y)\}^2 \, dxdy \Big/ \iint_{M} dxdy} \quad (7)$$

$$FOM_6 \equiv RMS \ of \ y \ Curvature \ Map = \sqrt{\iint_{M} \{\frac{\partial^2}{\partial y^2} error\_map(x,y)\}^2 \, dxdy \Big/ \iint_{M} dxdy} \quad (8)$$

where the surface integral limit M represents the error map surface. $M+$ and $M-$ are the error map areas with positive and negative residual error values, respectively. The six weighting factors can be adjusted depending on a specific purpose of a CCOS run as a design parameter.

The RMS deviation of the error map is calculated using FOM_1 and FOM_2. FOM_1 is the RMS of the positive error map, where the final surface is still higher than the target surface. FOM_2 is the RMS of the negative error map, where the final surface is lower than the target

surface. Because the polishing process can only remove material from the workpiece, the surface often needs to be kept higher than the target surface to a certain extent during the polishing process. This can be achieved by increasing the weighting factor C_2 for FOM_2. At the final polishing run to finish the project, both FOM_1 and FOM_2 may need to be minimized with the same weightings ($C_1 = C_2$) to minimize the conventional RMS of the error map.

The RMS deviation of the surface slope map [*i.e. FOM$_3$ & FOM$_4$* in Eq. (5) and (6)] and the RMS deviation of the surface curvature map [*FOM$_5$ & FOM$_6$* in Eq. (7) and (8)] are used to quantify the mid-spatial frequency error and localized small errors. The approaches using Fourier transform or PSD based figure of merits were excluded due to their computing power requirements. In contrast, the differential calculations in FOM_3, FOM_4, FOM_5 and FOM_6 can be easily done for a numerical data set (*e.g.* matrix for a pixelized error map) in most computing language platforms, such as MATLAB^{TM}.

The total figure of merit FOM_{total} combines the functions FOM_{1-6} with appropriate weighting coefficients depending on the purpose of a CCOS run, and provides a good criterion to optimize a CCOS run using a TIF library. For instance, if large C_3 and C_4 values were entered, the optimization engine would try to minimize the slope errors on the final workpiece. By minimizing FOM_{total}, the non-sequential optimization engine prevents the unwanted mid-spatial frequency error and localized small errors, while it achieves a small RMS of the residual error map.

4. Performance

4.1 High figuring efficiency

The figuring efficiency of a CCOS process can be maximized when an optimal TIF set is used for a given target removal. Four cases were simulated to demonstrate the performance of the non-sequential optimization. The figuring efficiency (*FE*) is defined by

$$FE \equiv \frac{RMS_{initial\_error\_map} - RMS_{residual\_error\_map}}{RMS_{initial\_error\_map}} \cdot 100 \qquad [\%]. \qquad (9)$$
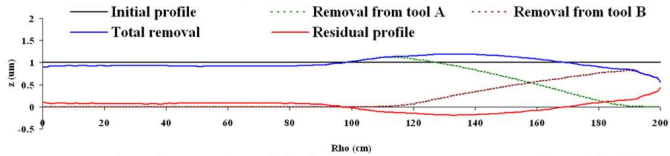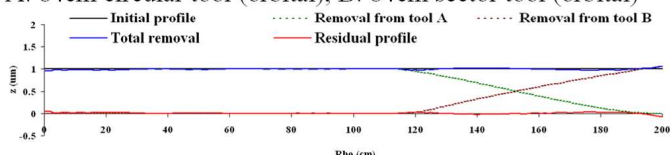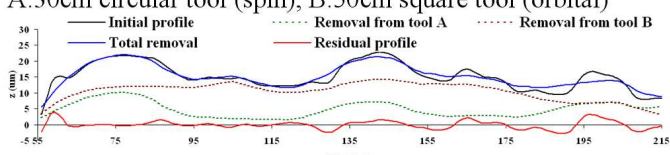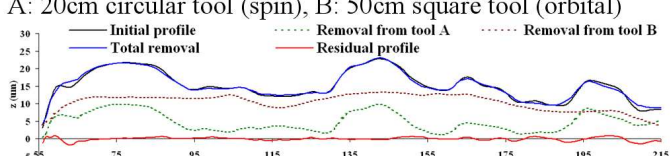
The advantage of performing the simultaneous optimization was demonstrated by comparing two case studies, Case 1.1 and 1.2. A 1μm piston target removal profile for a 2m radius workpiece was used. The piston target removal is often desired when one tries to remove sub-surface damages on a workpiece without changing the figure of the surface. A TIF using an 84cm circular tool with orbital tool motion was used as a primary TIF to achieve the target removal inside the workpiece edge. An 84cm sector tool was given for a secondary edge TIF. Only these two TIFs were used for both cases for a fair comparison, even though the non-sequential case may use other edge TIF as an optimal set with the primary TIF. The simulation results are presented in Fig. 3.

Case 1.1 did not use the non-sequential optimization technique. The given piston target removal was optimized using the primary TIF first. Then, the residual removal profile was optimized using the secondary edge TIF. The removal profile using the primary TIF (green dotted line in Case 1.1, Fig. 3) removed the target error to the edge as much as possible at the expense of having a bump around 100-120cm radial region. Also, the residual removal profile was not matched well with the removal using the secondary TIF (brown dotted line in Case 1.1, Fig. 3), so that the secondary TIF could not perform its role well. This is because the first optimization using the primary TIF did not consider the possible removal using the secondary TIF in the following optimization. This is a good example to show the fundamental limitation of the sequential approach. Finally, the residual profile shows relatively low figuring efficiency, *FE* = 88%, since those two TIFs were not utilized in a constructive manner.

Case 1.2 was optimized using the non-sequential optimization technique, where both the primary and secondary TIFs were considered simultaneously during the optimization process. Thus, the primary TIF intentionally left the edge side error, which was fit with the secondary edge TIF from the 84cm sector tool. As a result, a high figuring efficiency (*FE* = 98.4%) was accomplished. The two removal profiles from both TIFs (green and brown dotted lines in

Case 1.2, Fig. 3) matched well, so that the total removal (blue solid lines in Case 1.2, Fig. 3) is almost a constant (*i.e.* piston) removal profile. The residual error (red solid line in Case 1.2, Fig. 3) shows flat profile, which is much improved over Case 1.1.

Case No.	NS mode [a]	Utilized polishing tools (with tool motion) and radial profiles	RMS_{ini}, RMS_{res}, FE [b]
1.1	off (2)	A: 84cm circular tool (orbital), B: 84cm circular tool (orbital)	1μm 0.12μm 88%
1.2	on (2)	A: 84cm circular tool (orbital), B: 84cm sector tool (orbital)	1μm 0.016μm 98.4%
1.3	on (2)	A:30cm circular tool (spin), B:50cm square tool (orbital)	15.71μm 1.30μm 91.7%
1.4	on (5)	A: 20cm circular tool (spin), B: 50cm square tool (orbital)	15.71μm 0.50μm 96.8%

[a] NS mode means the non-sequential optimization mode. The number in the parenthesis refers the number of TIFs in the library.
[b] RMS_{ini} and RMS_{res} is the RMS of the initial and residual profile, respectively. FE is the figuring efficiency in Eq. (9).

Fig. 3. Optimization results for Case 1.1-1.4

Two more case studies were conducted to show the value of an optimal TIF set. For Case 1.3 and 1.4, a target removal profile for a 4.3m diameter surface was randomly generated. It has a 0.55m in radius circular hole at the center. This profile is shown as black solid lines (*i.e.* initial profile) in Case 1.3 and 1.4, Fig. 3. The TIF from 50cm square tool with orbital tool motion was given as a common primary TIF.

Case 1.3 was optimized using a secondary TIF from a 30cm circular tool with spin tool motion. The TIF library only had these two TIFs (using the 50cm primary square tool and 30cm circular tool), so that the optimization engine was not allowed to use other TIFs. Case 1.3 in Fig. 3 shows the optimized removal profiles using the 30cm circular tool (green dotted line) and the 50cm square tool (brown dotted line), which was not a good TIF set for the given target error profile. As shown in the residual profile (red solid line in Case 1.3, Fig. 3), most of the localized small errors in the target error profile were not removed since the secondary TIF from the 30cm circular tool was too large to remove them. The un-matched TIFs results in the relatively low figuring efficiency (*FE* = 91.7%) with hard-to-correct bumpy features on the residual error profile.

Case 1.4 was optimized using five TIFs (using the 50cm primary square tool and 10, 20, 30, 40cm circular tools) in the TIF library. For the direct comparison with Case 1.3 the final number of utilized TIFs was limited to two. As the result of the optimization, a TIF from a 20cm circular tool with spin tool motion was used as the secondary TIF. As you see in the removal profile using the 50cm tool (brown dotted line), the large tool removes most of the low-spatial frequency errors in the target error profile efficiently. Then, the removal profile from the 20cm tool (green dotted line) covers the localized small errors only. Most of the target errors were successfully removed with high figuring efficiency, $FE = 96.8\%$.

The comparison between Case 1.1 and 1.2 clearly shows the importance of the simultaneous optimization to achieve high figuring efficiency. Also, Case 1.4 highlights the advantage of utilizing an optimal TIF set for a given target removal.

4.2 Mid-spatial frequency error suppression with high time-efficiency

The performance of the non-sequential optimization technique for the suppression of mid-spatial frequency error (*i.e.* tool marks) was evaluated in a two-dimensional simulation of polishing the 1.6m New Solar Telescope (NST) primary mirror [27]. A 1.6m optical surface map with 701nm RMS of irregular errors was simulated as shown in Fig. 4. The target specification for the residual error map was set as <20nm RMS, the NST primary final optical surface specification [27].
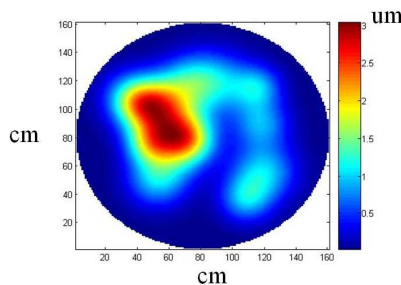

Fig. 4. Randomly generated 1.6m target removal map (surface RMS: 701nm, slope error RMS: 0.522arcsed, error volume: 1.31cm^3)

Due to uncertainties in the actual TIF shapes (including magnitude) and the tool positioning accuracy of the CCPM, the difference between the ideal removal and actual removal tends to produce the mid-spatial frequency error (*i.e.* tool marks) on the finished optical surface.

Large TIFs, which usually have less total dwell time with shorter tool path, are less sensitive to those uncertainties, so that the residual tool marks are limited. However, small TIFs are required to correct localized small errors. Thus, the key for the mid-spatial frequency error suppression is using proper size TIFs for various spatial frequency error components on the workpiece. The non-sequential optimization engine utilizes large and small TIFs for the low-spatial frequency errors and localized small errors, respectively.

For a realistic polishing simulation, we assumed random positioning errors and TIF magnitude variation. Up to 0.5% (of the workpiece size) tool positioning error was used. This positioning error may come from a low resolution measured target removal map, which may have errors in absolute coordinates, or a limited positioning accuracy of the CCPM itself. Up to ± 2.5% random variation in the TIF magnitude was applied during the simulations. This variation is a function of TIF stability, which is a characteristic of each tool. An actual laboratory environment may cause other errors which may degrade the simulation result. The simulation parameters are listed in Table 1.

Table 1. Parameters for the polishing simulation

Parameter	Values	Note
Target form accuracy	<20nm RMS	NST Spec [27].
Available tool sizes	100~300mm	Circular tools
Variation of TIF magnitude	± 2.5%	
Positioning error	± 4mm	0.5% of 1.6m

Three simulations were compared to show the performance of the non-sequential optimization technique in suppressing the mid-spatial frequency error. For the first two cases, Case 2.1 and 2.2, the non-sequential optimization technique was not used. Only a single TIF from the largest tool (300mm in diameter) or the smallest tool (100mm in diameter) was used during the polishing simulations. Case 2.3 utilized multiple TIFs simultaneously. The residual error maps and optimization results are summarized in Fig. 5 and Table 2.

[c] The accompanying movie clips (Media 1-3) show the evolution of the optical surface during the polishing process.
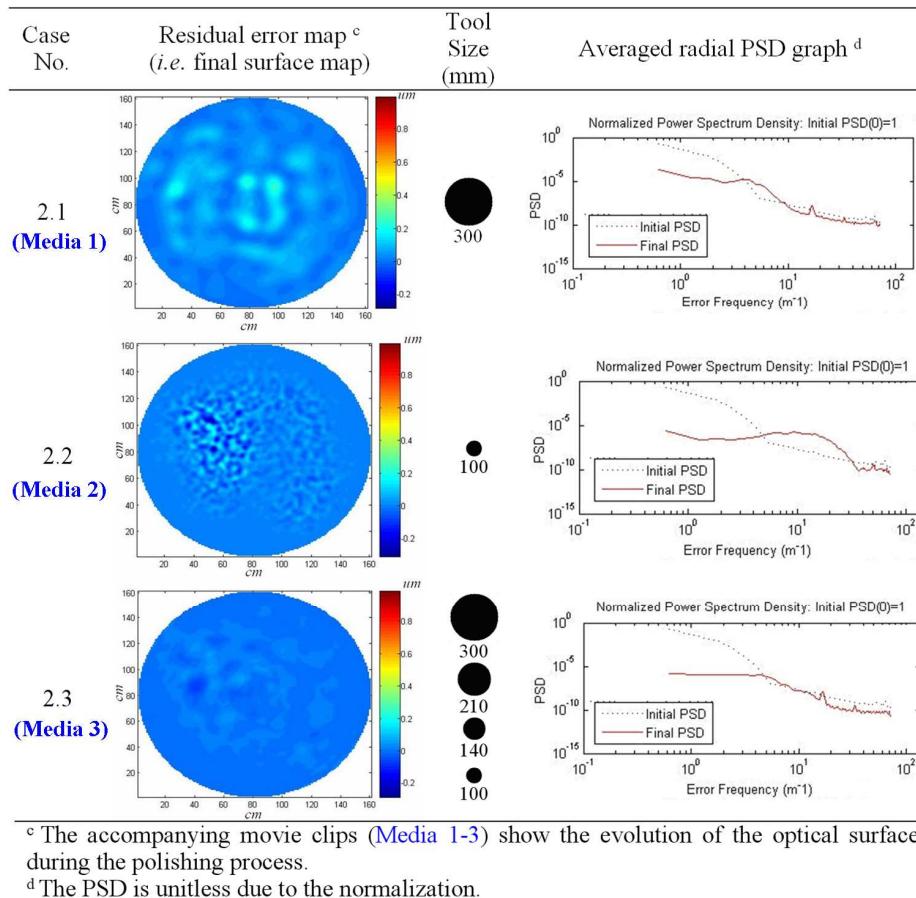[d] The PSD is unitless due to the normalization.

Fig. 5. (Media 1, Media 2, Media 3) Three simulation results for 1.6m NST target removal map.

Table 2. Surface specifications before and after polishing process for Case 2.1-2.3 [e]

Case No.	Initial surface spec. (*i.e.* target error map spec.)			Final surface spec. (*i.e.* residual error map spec.)			Total polishing time (unit time [f])
	Surface error RMS (nm)	Slope error RMS (arcsec)	Error volume (cm³)	Surface error RMS (nm)	Slope error RMS (arcsec)	Error volume (cm³)	
2.1	701	0.522	1.31	36 *94.9%*	0.1 *80.8%*	0.072 *94.5%*	82
2.2	701	0.522	1.31	31 *95.6%*	0.277 *46.9%*	0.006 *99.5%*	774
2.3	701	0.522	1.31	10 *98.6%*	0.057 *89.1%*	0.005 *99.6%*	100

[e] Percentile in *italic* represents the improvement ratio with respect to the initial surface specification for the surface error RMS, slope error RMS, and error volume. This is same as the figuring efficiency *FE* for the surface error RMS case.
[f] The 'unit time' was used for the relative comparison between cases.

The largest TIF, Case 2.1, left localized small errors on the final surface as shown in Fig. 5. There was a limitation caused by the small features ($>3m^{-1}$ in the PSD graph) which were relatively smaller than the TIF size. In contrast, for the Case 2.2, almost 99.5% of the form error volume was removed using the smallest TIF. However, it caused significant mid-spatial frequency error on the final optical surface. This is easily observed by comparing the initial and final PSD graphs in Case 2.2, Fig. 5. Even though the low-spatial frequency errors ($<5m^{-1}$) were removed, there was a significant generation of mid-spatial frequency error (5-$30m^{-1}$). As a result, the final RMS slope error was 0.277arcsec which was the worst among three cases in Table 2.

The non-sequential optimization result, Case 2.3, showed the best performance in terms of both preventing the mid-spatial frequency error and achieving the high figuring efficiency. The optimization engine used four different TIF diameters, 100, 140, 210 and 300mm, among the available TIF sizes between 100 and 300mm. The PSD graph (in Case 2.3, Fig. 5) shows good suppression (*i.e.* no increase from the initial PSD) in the mid-spatial frequency range (5-$30m^{-1}$) during the polishing process. This also means that the figures of merit in Section 3.4 were effectively representing the errors in terms of the spatial frequencies in the course of the optimization. The final surface had 0.057arcsec RMS slope variation and 10nm RMS surface irregularity, which meets the target specification. About 99.6% of the initial error volume was removed. This demonstrates that the non-sequential optimization technique successfully balanced between various size TIFs by selecting the large TIFs for most of the error volume and the small TIFs only for the localized small errors. The final surface error map is shown in Case 2.3, Fig. 5.

As shown in Table 2, the total polishing time for non-sequential optimization Case 2.3 (100 unit time) was much smaller compared to the 774 unit time of Case 2.2. While both Case 2.1 and 2.3 show significantly shorter total polishing time, Case 2.3 which used multiple TIFs resulted in superior performance. Thus, the non-sequential optimization technique provides a time-efficient CCOS process with both high figuring efficiency and good mid-spatial frequency error suppression.

5. Concluding remarks

In this paper the non-sequential optimization technique for a CCOS process utilizing multiple TIFs was developed and its performance was demonstrated. This technique benefits from the use of a wider search space (including the tool shape, tool size, and so forth) than that of conventional optimization techniques. An optimal TIF set for a given target removal is suggested as an optimization result, so that high ($>95\%$) figuring efficiency can be achieved. Also, the simulations showed that the CCOS process equipped with the new optimization technique effectively suppresses the mid-spatial frequency error. About 89% reduction in the

slope error RMS was successfully demonstrated in the Case 2.3 simulation. The high time-efficiency (*i.e.* short polishing time) of the CCOS process using the new technique was clearly demonstrated. The CCOS aided with this new optimization technique enables mass fabrication processes for high quality optical surfaces, and will meaningfully contribute to the materialization of the next generation optical systems, such as Laser Inertial Fusion Engine [28] and ELT projects [12–16].

Appendix A. TIF library

Table 3. Parameters for the TIF library generation [g]

TIF No.	Tool RPM [h]	Workpiece RPM [h]	Tool width [i] (cm)	Tool motion	Orbital motion radius [j] (cm)	Tool Shape
1	1	<<1	60	Spin	N/A	Circle
2	1	<<1	60	Spin	N/A	Donut
3	1	<<1	60	Orbital	15	Circle
4	1	<<1	60	Orbital	10	Circle
5	1	<<1	60	Orbital	10	Square
6	1	<<1	60	Orbital	10	Rectangle
7	1	<<1	60	Orbital	5	Sector
8	1	<<1	60	Orbital	5	Sector
9	1	<<1	60	Orbital	10	Ellipse
10	1	<<1	60	Orbital	12	Donut
11	1	2.00	60	Spin	N/A	Circle
12	1	1.00	60	Spin	N/A	Circle
13	1	0.50	60	Spin	N/A	Circle
14	1	0.10	60	Spin	N/A	Circle
15	1	0.05	60	Spin	N/A	Circle
16	1	−0.05	60	Spin	N/A	Circle
17	1	−0.10	60	Spin	N/A	Circle
18	1	−0.15	60	Spin	N/A	Circle
19	1	−0.20	60	Spin	N/A	Circle
20	1	−1.00	60	Spin	N/A	Circle
21	1	1.50	70	Spin	N/A	Circle
22	1	1.50	60	Spin	N/A	Circle
23	1	1.50	50	Spin	N/A	Circle
24	1	1.50	40	Spin	N/A	Circle
25	1	1.50	30	Spin	N/A	Circle
26	1	1.50	60	Orbital	20	Circle
27	1	1.50	60	Orbital	15	Circle
28	1	1.50	60	Orbital	10	Circle
29	1	1.50	60	Spin	N/A	Circle
30	1	1.50	50	Spin	N/A	Circle

[g] Preston constant [9] was assumed as −100μm/psi(m/sec)hour with 1 PSI tool pressure.
[h] Positive and negative RPM means clockwise and counterclockwise rotation, respectively.
[i] Tool width is measured in max direction.
[j] Orbital motion radius refers to the radius of the circle passing through the points A~F in Fig. 1 (left).
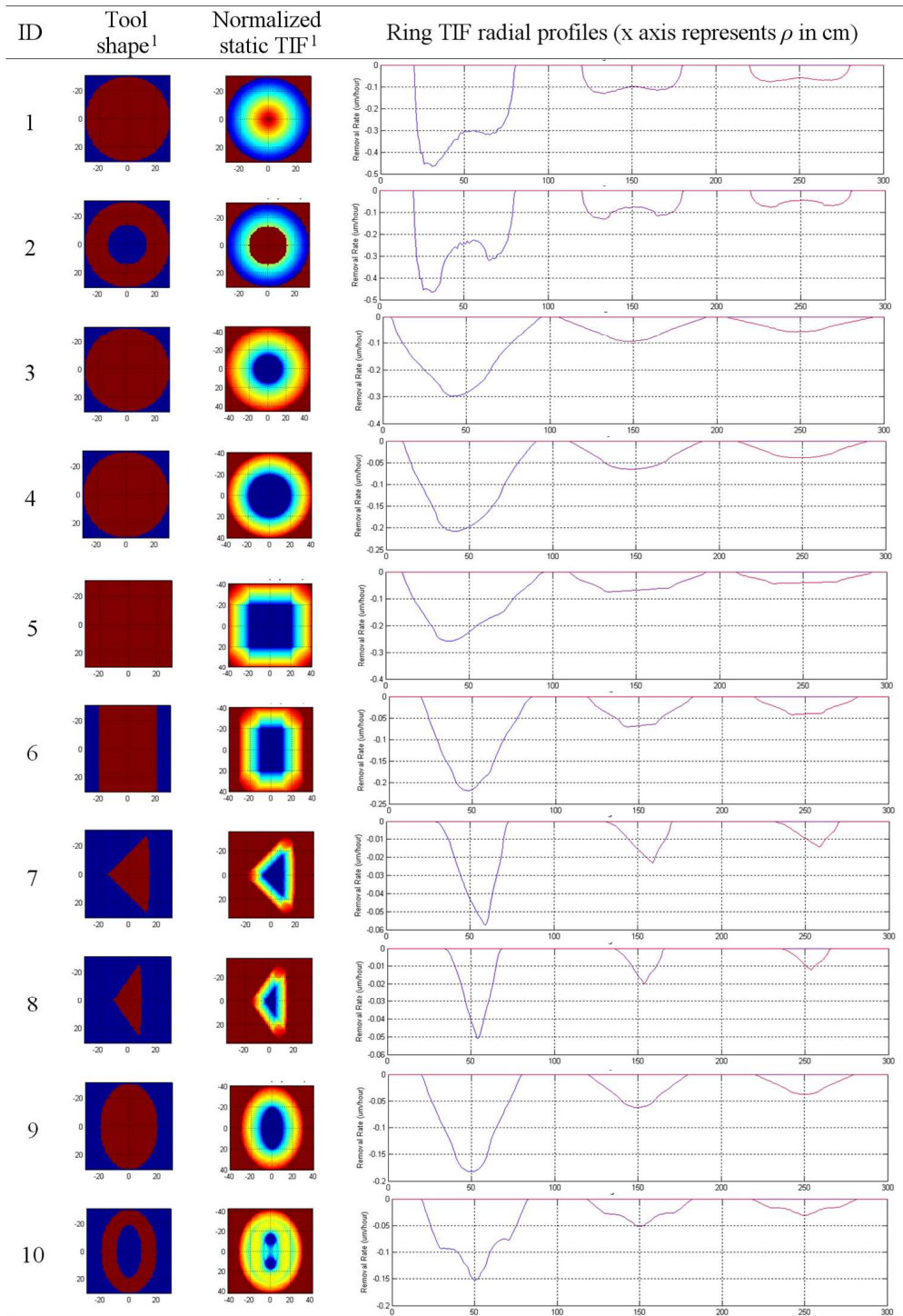
ID	Tool shape[1]	Normalized static TIF[1]	Ring TIF radial profiles (x axis represents ρ in cm)
1			
2			
3			
4			
5			
6			
7			
8			
9			
10			

Fig. 6. Complementary TIF library

ID	Tool shape[1]	Normalized static TIF[1]	Ring TIF radial profiles (x axis represents ρ in cm)
11			
12			
13			
14			
15			
16			
17			
18			
19			
20			

Fig. 6. Complementary TIF library (*continued*)

ID	Tool shape[1]	Normalized static TIF[1]	Ring TIF radial profiles (x axis represents ρ in cm)
21			
22			
23			
24			
25			
26[k]			
27[k]			
28[k]			
29[k]			
30[k]			
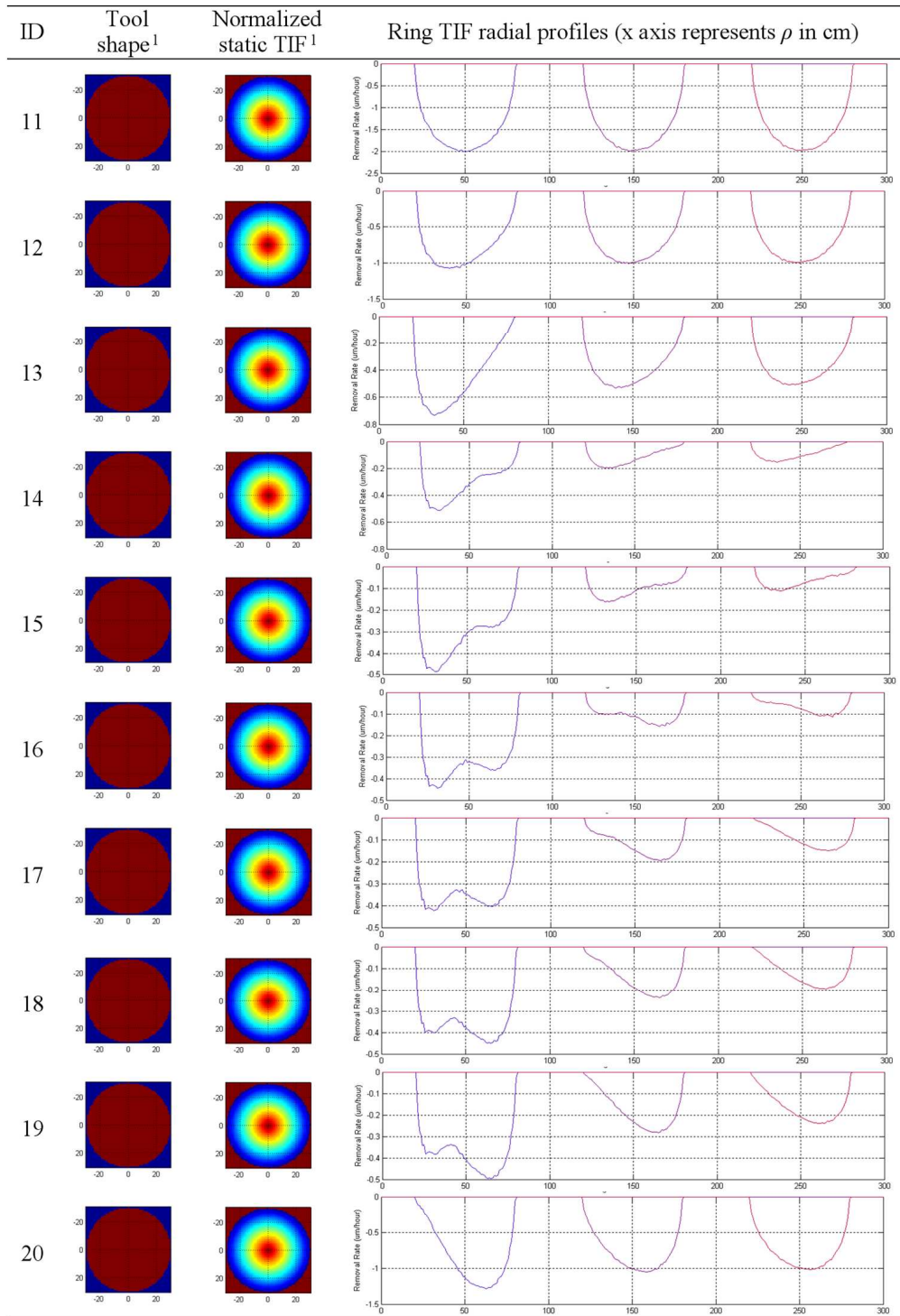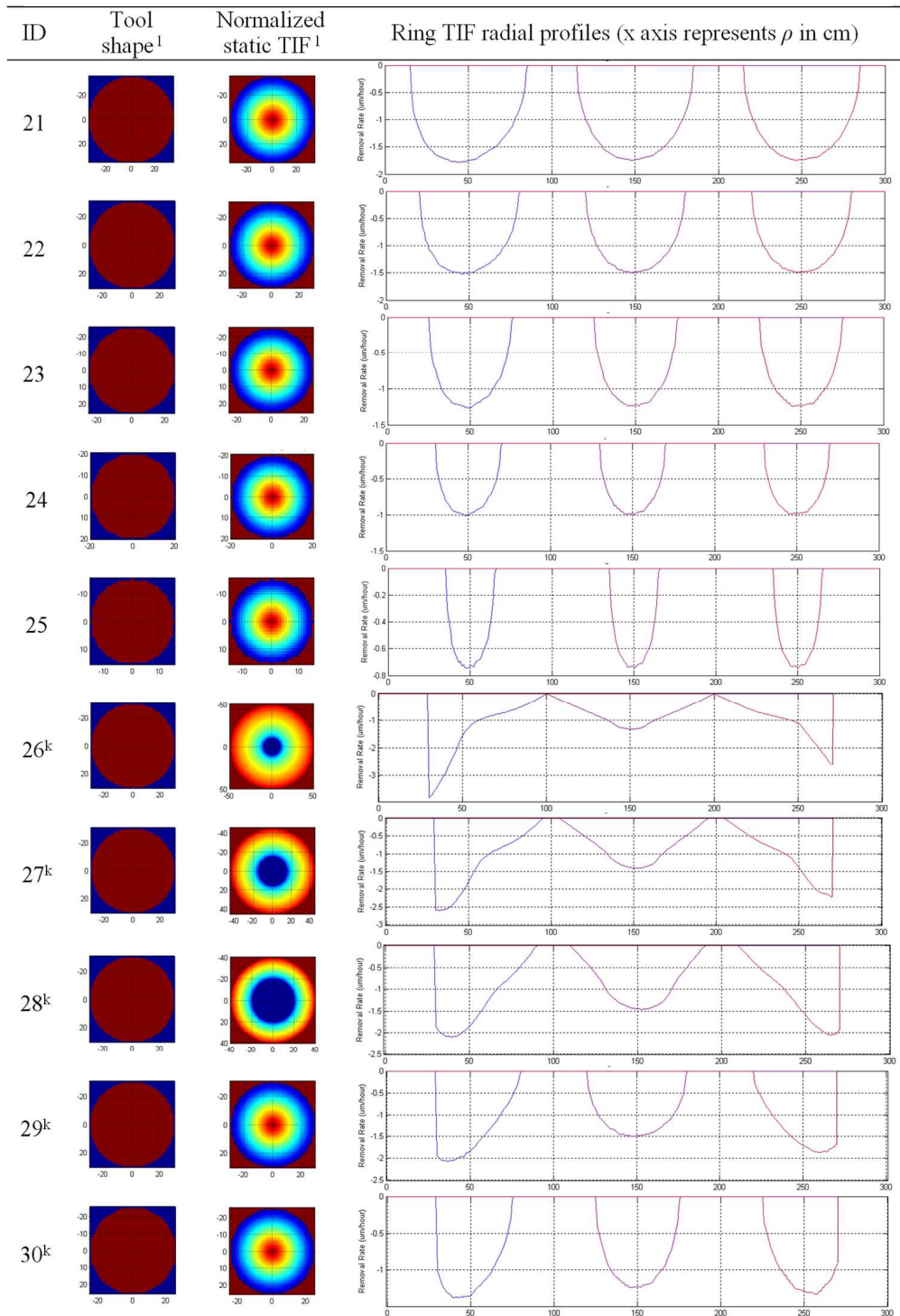
[k] The parametric edge model [19] was used to calculate the edge TIFs for the TIF No. 26-30. Workpiece inside and outside edge was at 30 and 270cm, respectively.
[1] The units for the tool shape and the normalized static TIF are in cm.

Fig. 6. Complementary TIF library (*continued*)

Appendix B. Analytical solution for the dwell time map

The analytical solution for the dwell time map in Eq. (1) does not exist in general. The main reason is that the CCOS process is not a Linear Shift Invariant (LSI) system. For a LSI system, the TIF (*i.e.* impulse response) should not be a function of workpiece coordinates $x_{workpiece}$ and $y_{workpiece}$ [29]. The TIF should be same everywhere on the workpiece.

Conventional CCOS often assumes a LSI system (*i.e.* spatially invariant TIF) [20,22,30] by assuming, i) the velocity of the workpiece motion is small enough compare to the tool motion and ii) there is no edge effect. In this case, by replacing the $TIF(x_{TIF},\ y_{TIF},\ x_{workpiece},\ y_{workpiece})$ with $TIF(x_{TIF},\ y_{TIF})$ in Eq. (1), the analytical solution for the dwell time map can be calculated using the property of Fourier transform as below. (The 2D convolution operator can be changed to the multiplication operator.)

$$
\begin{aligned}
&\mathrm{FF}[Removal\_map(x_{workpiece}, y_{workpiece})] \\
&= \mathrm{FF}[Dwell\_time\_map(x_{workpiece}, y_{workpiece}) ** TIF(x_{TIF}, x_{TIF})] \\
&= \mathrm{FF}[Dwell\_time\_map(x_{workpiece}, y_{workpiece})] \cdot \mathrm{FF}[TIF(x_{TIF}, x_{TIF})]
\end{aligned}
\qquad (10)
$$

where *FF* is the 2D Fourier transform. Then, using the inverse Fourier transform, the dwell time map is

$$
\begin{aligned}
&Dwell\_time\_map(x_{workpiece}, y_{workpiece}) \\
&= \mathrm{FF}^{-1}[\frac{\mathrm{FF}[Removal\_map(x_{workpiece}, y_{workpiece})]}{\mathrm{FF}[TIF(x_{TIF}, x_{TIF})]}] \\
&= \mathrm{FF}^{-1}[\frac{\mathrm{FF}[Target\_removal\_map(x_{workpiece}, y_{workpiece})]}{\mathrm{FF}[TIF(x_{TIF}, x_{TIF})]}]
\end{aligned}
\qquad (11)
$$

where FF^{-1} is the inverse 2D Fourier transform. The removal map is replaced with the target removal map, which is the ideal goal. This is an analytical and ideal dwell time map solution, which gives the perfect removal map.

However, the analytical solution cannot be used as it is. The analytical dwell time map solution in Eq. (11), in general, may result in negative values that are unrealistic. A negative dwell time means that the tool would add material to the workpiece surface. Another practical issue comes when we use the numerical techniques to compute the Fourier transform, such as Fast Fourier transform (FFT). Because all functions should be limited in a finite range in any computational environment, the analytical solution is often not valid especially for the edge regions of the workpiece.

Also, the LSI assumption is not valid for the non-sequential CCOS optimization. Instead, the TIF should be handled as a function of position on the workpiece. For instance, the edge TIFs are very strong function of overhang distance over the edge of the workpiece [19]. Also, if the TIF shape is not axisymmetric (*e.g.* square tool case) and the workpiece rotates, the orientation of the square TIF also rotates with respect to the workpiece. Thus, no general solution to the dwell time map in Eq. (1) exists analytically.

Acknowledgments